Poroelastic effects destabilize mildly rate-strengthening friction to generate stable slow slip pulses

Elías R. Heimisson[a,*], Eric M. Dunham[a,b], Martin Almquist[a]

[a]*Department of Geophysics, Stanford University, Stanford, California, USA*
[b]*Institute for Computational and Mathematical Engineering, Stanford University, Stanford, California,*
USA

Abstract

Slow slip events on tectonic faults, sliding instabilities that never accelerate to inertially limited ruptures or earthquakes, are one of the most enigmatic phenomena in frictional sliding. While observations of slow slip events continue to mount, a plausible mechanism that permits instability while simultaneously limiting slip speed remains elusive. Rate-and-state friction has been successful in describing most aspects of rock friction, faulting, and earthquakes; current explanations of slow slip events appeal to rate-weakening friction to induce instabilities, which are then stalled by additional stabilizing processes like dilatancy or a transition to rate-strengthening friction at high slip rates. However, the temperatures and/or clay-rich compositions at slow slip locations are almost ubiquitously associated with rate-strengthening friction. In this study, we propose a fundamentally different instability mechanism that may reconcile this contradiction, demonstrating how slow slip events can nucleate with mildly rate-strengthening friction. We identify two destabilizing mechanisms, both reducing frictional shear strength through reductions in effective normal stress, that counteract the stabilizing effects of rate-strengthening friction. The instability develops into slow slip pulses. We quantify parameter controls on pulse length, propagation speed, and other characteristics, and demonstrate broad consistency with observations of tectonic slow slip events as well as laboratory tribology experiments.

Keywords: friction, stability and bifurcation, geological material, porous material, slip pulses

1. Introduction

Frictional instabilities are intrinsically linked with shear fracturing and material failure[1]. Earthquakes are notable examples of such instabilities, featuring explosive, inertially limited rupture growth on faults following gradual development of instability. Yet not all faults slip in earthquakes; some slide steadily in response to tectonic loading. This diversity in sliding behavior is well explained by rate-and-state friction, an experimentally based description of how the friction coefficient, f, evolves with sliding velocity (i.e., slip rate, V) and sliding history. The fault shear strength $\tau = f(\sigma - p)$, the product of friction coefficient f and effective normal stress, the difference between compressive total stress σ and pore fluid pressure p. It is widely thought[2] that instabilities during sliding require rate-weakening friction, in which f decreases with increasing V (following a transient rate-strengthening response that stabilizes short-wavelength perturbations). Likewise, rate-strengthening friction is linked to aseismic slip, which is thought to occur steadily in the absence of changes in loading.

Slow slip events are challenging to reconcile with this understanding. Slow slip occurs in subduction zones and possibly at the base of some strike-slip faults and is one component of a class of sliding events that includes low-frequency earthquakes, tectonic tremor, tsunami earthquakes, some landslides, and even stick-slip cycles on ice streams[3, 4]. Slow slip is also thought to play an important role in injection-induced seismicity and reservoir stimulation by hydraulic fracturing[5, 6]. In addition, slow slip has been observed in friction experiments, in particular experiments on hydrogels that report spontaneous nucleation of slip pulses that propagate faster than the loading speed but much slower than elastic wave speeds [7, 8, 9, 10, 11].

The challenge posed by slow slip events is to simultaneously explain their unstable nature (i.e., why the interface does not slide steadily) and why they do not continue to grow into ruptures. Current theories posit that slow slip events nucleate under rate-weakening friction, just like earthquakes, but then stall for a variety of reasons. These include a transition from rate-weakening to rate-strengthening friction with increasing V, stabilization by dilatancy,

---

*Corresponding author:
Email address: `eliasrh@stanford.edu` (Elías R. Heimisson)

and interaction with frictional heterogeneities[12, 13, 14, 15, 16]. However, these theories are inconsistent with indications that slow slip occurs in regions with rate-strengthening friction, based on temperature conditions and/or clay-rich compositions[17, 18, 19, 20].

In this paper, we show that slow slip arises naturally from instabilities with mildly rate-strengthening friction. These instabilities arise from two distinct mechanisms, both involving configurations where slip couples to changes in effective normal stress $\sigma - p$. The first mechanism occurs during sliding between poroelastic solids, for which compression or dilation of material causes changes in pore pressure p that alter frictional strength τ on the sliding interface [21, 22, 23] The second mechanism arises during sliding at the interface between two dissimilar elastic solids, a process that alters total normal stress σ on the interface and hence frictional strength τ [24]. We focus primarily on the poroelastic mechanism, but point out a correspondence between the undrained poroelastic problem and the elastic bimaterial problem (at least for a linearized friction law). We identify and characterize the sliding instabilities through 1.) linear stability analysis of perturbations about steady sliding, and 2.) numerical simulations of nucleation and propagation of slip pulses with fully nonlinear rate-and-state friction. Both the stability analysis and numerical simulations are done for linear poroelastic solids.

This paper has four main sections. In Section 2 we present the conceptual and mathematical model. In Section 3 we develop solutions and discuss results for linearized rate-and-state friction on a slip surface in a poroelastic medium. Specifically, we derive a characteristic equation that describes the stability of the slip surface to a Fourier mode perturbation. Section 4 describes numerical simulations that account for fully nonlinear frictional response. Finally, Section 5 discusses and interprets the results in the context of observations of slow slip in nature and laboratory experiments; furthermore, we speculate on the manifestation of the rate-strengthening instability in 3D with possible application to subduction zone slow slip events and other geological phenomena.

3

2. Model

In this section we elaborate on the conceptual, mathematical, and physical foundations of the model before presenting the linearized stability analysis and numerical simulations that will follow.

2.1. Fault structure, poroelastic effects, and coupling to fault strength

The mechanical and physical properties of the fault core, a region of the fault zone of high strain where slip localizes (Fig. 1a-b), are important to understanding how slip nucleates and propagates on natural faults. Fault cores are mechanically and chemically different from the surrounding damage zone and, beyond that, the intact host rock. The fault core is thin compared to many seismologically relevant length scales, having a thickness (w in Fig. 1b) ranging from a few centimeters to meters [25]. Fault cores in well-developed fault zones often have very low permeability [26, 27, 28] compared to the surrounding damage zone and host rock [29, 30]. It is worth noting that in the analysis of this paper, we will use the concept of a fault core to describe a thin layer, in which slip localizes, with different mechanical and hydrological properties than the surrounding medium. However, in nongeological applications, the fault core may be regarded as a tribofilm that is produced by long-term wear of the frictional interface.

In this study, we assume that slip has localized at the boundary of the fault core (Fig. 1a-b), a configuration that maximizes the potential for instability compared to other locations within the fault core, as shown subsequently. Field exposures of formerly active faults also often feature localization on one side of the core [31, 32, 33].

Spatially nonuniform slip in this configuration compresses material on one side of the interface and dilates it on the opposite side, altering fluid pressure through poroelastic coupling [21, 22, 23, 34, 35]. Furthermore, this process is asymmetric, with pore pressure increases on one end of a slipping zone matched by corresponding decreases in pore pressure on the opposite end. The relatively impermeable fault core delays pressure equilibration by flow across the core. These changes in pressure cause changes in the effective normal stress on the slip surface that asymmetrically alter the shear strength of the fault[23, 34, 35].

Slip localization to the boundary of the core thus gives rise to an asymmetry that favors propagation in one direction, with the favorable direction determined by which boundary of the core hosts the slip surface. A related bimaterial effect altering normal stress occurs during sliding between elastically dissimilar solids [24, 36, 37, 38]. The strong sense of directionality in both the poroelastic and elastic bimaterial problems is a characteristic property of slip pulses (Fig. 1c). Experiments confirm that slip instabilities on poroelastic and/or elastic bimaterial interfaces often develop into propagating slip pulses [9, 39]. Coupling of slip to normal stress is not unique to poroelastic and bimaterial interfaces. Interfaces of elastic materials with identical mechanical properties also produce such coupling if the materials lack geometric reflection symmetry[40].

In this study, we consider sliding on a slip surface at the edge of a fault core of width w with mobility (permeability divided by fluid viscosity) κ_c. The rock outside the fault core has a possibly different mobility κ. For simplicity, we do not distinguish between the damage zone and host rock in this study.

2.2. Linear poroelasticity

Here we describe the governing equations of quasi-static linear isotropic poroelasticity and the interface conditions that we impose in our problem. The displacements u_i and pressure changes p are governed by a set of four coupled partial differential equations. Assuming that body forces are negligible, these are [e.g. 41]

$$Gu_{i,kk} + \frac{G}{1-2\nu}u_{k,ki} = \alpha p_{,i} \tag{1}$$

and

$$\frac{1}{M}p_{,t} - \kappa p_{,kk} = -\alpha u_{k,kt}, \tag{2}$$

where summation over repeated indices is implied and subscript $,t$ denotes the partial time derivative and $,k$ denotes the partial spatial derivative in direction x_k. The material parameters are the shear modulus G, drained Poisson ratio ν, mobility κ, Biot-Willis coefficient α, and Biot modulus M. From Eq. 1 we see that the scaled pore pressure gradient, $\alpha p_{,i}$, acts
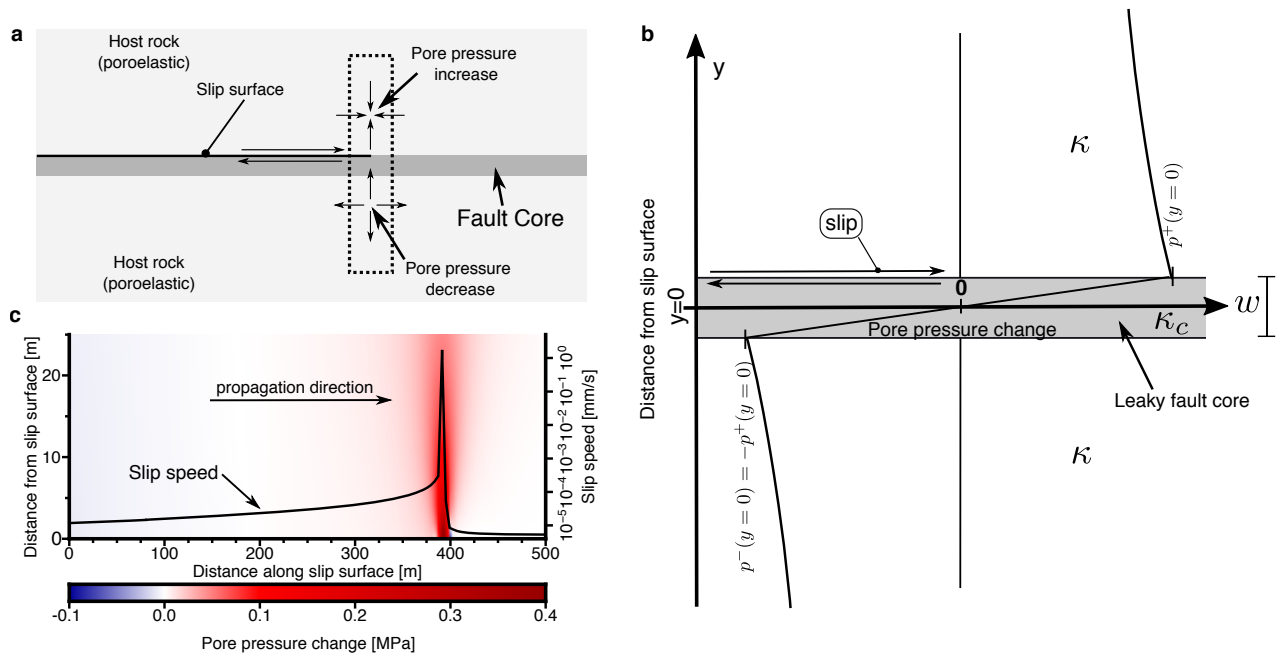
5

Figure 1: **a** Schematic of fault zone with slip localized on one side of the low permeability core, idealized in our study as having infinitesimal width with respect to the perturbation wavelength λ. Pressure changes are caused by compression/dilation of the near-fault material. **b** Zoomed-in view of dashed box in **a**, showing pore pressure change (with respect to a positive initial value) across the sliding interface. For across-fault diffusion we consider the core to have thickness $w \ll \lambda$ and mobility κ_c, which may be different from the mobility κ of the surrounding rock. **c** Simulated slow slip pulse (black line with scale on the right axis) from Section 4; elevated pore pressure around the slip front weakens the interface, facilitating propagation.

as an effective body force. In Eq. 2, the scaled dilation rate, $-\alpha M u_{k,kt}$, is a source term to a diffusion equation for pore pressure. The Biot-Willis parameter α (between 0 and 1) establishes the two-way coupling between the pore fluid phase and the elastic solid matrix. We refer to Detourney and Cheng [41] for more detailed discussion of various poroelastic parameters. In other sections, different sets of five parameters will be introduced if they provide simpler expressions. Specifically, we use Skempton's coefficient B, the undrained Poisson ratio ν_u, and the hydraulic diffusivity $c = \kappa M$. Note that B relates undrained response in pore pressure p perturbations to changes in mean stress: $p = -B\Delta\sigma_{kk}/3$ [22] and is always between 0 and 1. We may relate B and ν_u to the material parameters in Eqs. 1 and 2 using the following equations:

$$B = \frac{3M\alpha(1 - 2\nu)}{2G(1 + \nu) + 3M\alpha^2(1 - 2\nu)}, \tag{3}$$

$$\nu_u = \frac{2G\nu + M\alpha^2(1 - 2\nu)}{2G + 2M\alpha^2(1 - 2\nu)}; \tag{4}$$

furthermore, a relationship between B and ν_u is given by

$$B = \frac{3(\nu_u - \nu)}{\alpha(1 - 2\nu)(1 + \nu_u)}. \tag{5}$$

In this study we seek a solution of Eqs. 1 and 2 for two half-spaces under the assumption of 2-D plane strain deformation, thus reducing the system to three coupled partial differential equations. We utilize an x-y Cartesian coordinate system with $y = 0$ being the sliding interface. Our first objective is to obtain linear relations between slip and stress and pressure change on the interface, which are used in subsequent sections when enforcing a specific interface friction law. To obtain these linear relations, the following boundary and interface conditions are imposed:

7

$$\lim_{y \to 0^\pm} u_x^+ - u_x^- = \delta, \tag{6}$$

$$\lim_{y \to 0^\pm} u_y^+ - u_y^- = 0, \tag{7}$$

$$\lim_{y \to \pm\infty} u_i^\pm = 0, \tag{8}$$

$$\lim_{y \to \pm\infty} p^\pm = 0, \tag{9}$$

$$\lim_{y \to 0^\pm} \sigma_{xy}^+ - \sigma_{xy}^- = 0, \tag{10}$$

$$\lim_{y \to 0^\pm} \sigma_{yy}^+ - \sigma_{yy}^- = 0, \tag{11}$$

where superscripts $+$ or $-$ represent the upper ($y > 0$) or lower ($y < 0$) half-spaces. The first equation imposes slip δ across the interface. The second equation assures that no opening or interpenetration occurs on the interface. The third requires displacements and stresses to vanish at infinity; the fourth requires pore pressure changes and fluid flux to also vanish at infinity. The fifth and sixth equations enforce Newton's third law across the interface. Two more conditions are required on the fault to fully specify the problem, which describe the pore pressure or flux conditions on the interface. We formulate these conditions in Section 2.3. These boundary conditions are formulated to characterize perturbations around steady sliding and thus due not include far-field loading or prestress associated with compression of the medium and shear resistance to spatially uniform steady sliding. Furthermore, solutions to the linear problem stated above can be utilized together with a friction law that prescribes some relation between shear stress, normal stress, pore pressure, slip, slip rate, etc. Specifically, in Section 2.5 we combine these solutions with a linearized rate-and-state friction law.

2.3. Leaky fault model

We next introduce two pressure and fluid flow interface conditions on the slip surface. We assume that slip perturbations have wavelengths λ much larger than the fault core thickness w (Figure 1b). This scale separation, together with symmetry (or antisymmetry) of fields

8

across the fault, permits application of an approximate leaky fault model recently introduced by Song and Rudnicki[42]. The leaky fault model accounts for flow across the fault core via linear relations between pore pressure and its gradient in the fault-normal direction on the two sides of the slip surface:

$$\frac{dp^\pm}{dy}\bigg|_{y=0^\pm} = \pm\frac{\kappa_c}{\kappa}\frac{2p^\pm}{w}. \tag{12}$$

We note that if $\kappa_c/\kappa \to 0$ then $dp^\pm/dy \to 0$ at $y = 0^\pm$, thus providing boundary conditions corresponding to an impermeable fault core. However, if $\kappa/\kappa_c \to 0$ then $p^\pm \to 0$, which corresponds to a fully permeable fault core.

2.4. Solution of poroelastic problem with imposed slip

The governing equations and interface conditions (with imposed slip) can be solved analytically in the Fourier-Laplace domain. We carry out a Fourier transform in fault-parallel distance x and Laplace transform in time t; this joint transform is defined as

$$\hat{\delta}(s,k) = \int_0^\infty \int_{-\infty}^\infty \delta(t,x)e^{-ikx-st}dxdt \tag{13}$$

for slip and similarly for other fields. The procedure in Appendix A provides linear relations between the transformed shear stress change on the interface, $\hat{\tau}$, pore pressure change on the two sides of the interface, $\hat{p}^\pm$, and slip, $\hat{\delta}$:

$$\hat{\tau} = -\frac{G|k|\hat{\delta}}{2(1-\nu_u)}H_1(s,k) \tag{14}$$

and

$$\hat{p}^\pm = \mp\frac{ikGB\hat{\delta}}{3}\frac{1+\nu_u}{1-\nu_u}H_2(s,k), \tag{15}$$

where

$$H_1(s,k) = 1 - \frac{2(\nu_u-\nu)}{1-\nu}\frac{ck^2}{s}\frac{1+\mathcal{F}}{\mathcal{F}+\sqrt{1+s/ck^2}}\left(\sqrt{1+s/ck^2}-1\right), \tag{16}$$

and

$$H_2(s,k) = \frac{\sqrt{1+s/ck^2}-1}{\sqrt{1+s/ck^2}+\mathcal{F}}, \tag{17}$$

in which $\mathcal{F}$ is a nondimensional parameter (given a fixed k) that characterizes the importance of flux across the fault:

$$\mathcal{F} = \frac{\kappa_c}{\kappa}\frac{2}{|k|w}. \tag{18}$$

9

170   There is no change in total normal stress on the interface, $\hat{\sigma} = 0$.

171   Note that both $H_1(s, k)$ and $H_2(s, k)$ go to unity in the limit where $ck^2/s \to 0$ assuming

172   $\mathcal{F} < \infty$. We will refer to this as the undrained limit, where the change in effective normal

173   stress is the largest. We explore this limit later in detail due to mathematical simplicity and

174   the physically interesting effects that arise from changes in the effective normal stress. If

175   $\mathcal{F} \to \infty$, then $\hat{p}^{\pm} \to 0$, which corresponds to a fully permeable fault, in which case there is

176   no change in effective normal stress on the fault.

177   *2.5. Rate-and-state friction*

178   Frictional sliding on the slip surface is governed by rate-and-state friction, which provides

179   a relation between shear strength τ, effective normal stress $\sigma' = \sigma - p$, and friction coefficient

180   f that depends on sliding velocity V and state variable Ψ. The latter obeys a state evolution

181   equation.

182   In the first part of this study, we perform a linear stability analysis using a general form

183   of linearized rate-and-state friction, valid for small perturbations about a steady sliding

184   solution at slip speed V_0, that encompasses a broad class of steady state friction and state

185   solution laws[36]:

$$\frac{\mathrm{d}\tau}{\mathrm{d}t} = \frac{a\sigma_0'}{V_0}\frac{\mathrm{d}V}{\mathrm{d}t} + (f_0 - \alpha_{LD})\frac{\mathrm{d}\sigma'}{\mathrm{d}t} - \frac{V_0}{L}\left[\tau - f_0\sigma' - \frac{(a-b)\sigma_0'}{V_0}(V - V_0)\right], \qquad (19)$$

186   in which f_0 is the steady-state coefficient of friction at sliding velocity V_0, α_{LD} is the Linker-

187   Dieterich constant [43], L is the state evolution distance, $\sigma_0' = \sigma_0 - p_0$ is the initial effective

188   normal stress, and a and b are dimensionless parameters that are related to the rate and

189   state dependence of friction, respectively.

190   In the second part of this study, we perform simulations with nonlinear rate-and-state

191   friction. For this we set $\alpha_{LD} = 0$ and use a standard logarithmic dependence of steady state

192   friction coefficient on slip velocity together with the slip evolution law [e.g. 36]

$$f(V, \Psi) = a \operatorname{arcsinh}\left(\frac{V}{2V_0}e^{\Psi/a}\right), \qquad (20)$$

$$\frac{\partial \Psi}{\partial t} = -\frac{V}{L}\left[f - f_{ss}(V)\right], \qquad (21)$$

where σ' is the effective normal stress, the steady state friction coefficient is

$$f_{ss}(V) = f_0 + (a - b) \ln (V/V_0).$$
(22)

Friction is said to be rate-strengthening (under steady sliding conditions) if $a - b > 0$ and rate-weakening if $a - b < 0$. Linearization of Eqs. 20–22 yields Eq. 19.

2.6. Parameter values

For the analysis and simulations we present, we assume a set of reference parameters (Table 1), which are typical for many geological settings and problems. Unless otherwise explicitly stated they are kept constant throughout this study, but frequently we will vary one or more parameter systematically while maintaining the others as listed in Table 1.

3. Linear stability analysis

In this section we investigate the linear stability of steady state sliding at slip velocity V_0 to small Fourier mode perturbations. We assume that inertial effects can be neglected, which is valid if $GV_0/(2c_s a\sigma'_0) \ll 1$ where c_s is the S wave speed [36] (see also Table 1). The linear poroelastic solution developed in Section 2.2 is utilized to describe perturbations about the prestressed, steady sliding solution. We show that steady sliding with a low permeability fault core is conditionally unstable for mildly rate-strengthening friction, in the sense that that small amplitude perturbations can spontaneously grow to nucleate slip instabilities. Later we demonstrate how these instabilities evolve in quasi-dynamic simulations, under nonlinear friction effects, into propagating slow slip pulses.

3.1. Characteristic equation

Applying a Fourier transform in x and a Laplace transform in time, Eq. 19 is

$$\left(s + \frac{V_0}{L}\right)\hat{\tau} = \left[f_0\left(s + \frac{V_0}{L}\right) - \alpha_{LD}s\right]\hat{\sigma}' + \left[\frac{a\sigma'_0}{V_0}s^2 + \frac{(a - b)\sigma'_0}{L}s\right]\hat{\delta}.$$
(23)

Next we insert the linear poroelastic relations, Eqs. 14 and 15, into Eq. 23 and obtain the characteristic equation. Assuming slip localization on the $y > 0$ side of the interface (Fig. 1b), such that $\hat{\sigma}' = -\hat{p}^+$, the characteristic equation is

11

Table 1: Reference parameters

Symbol	Description	Value
Material properties		
B	Skempton's coefficient	0.6
ν	Drained Poisson's ratio	0.25
ν_u	Undrained Poisson's ratio	0.35
G	Shear modulus	30 GPa
Friction		
L	Characteristic state evolution distance	10 μm
a	Rate dependence of friction	0.01
$a - b$	Degree of rate-strengthening	1.5×10^{-4}
α_{LD}	Linker-Dieterich constant [43]	0
V_0	Steady state sliding velocity	10^{-9} m/s
f_0	Steady state coefficient of friction at V_0	0.6
σ'_0	Initial effective normal stress	50 MPa
Nondimensional parameters		
γ	Lateral diffusion stabilization	0.08
ϵ	Across fault flow stabilization (Eq. 28)	0
Physical scales — dependent on parameters above		
λ_c	Approximate preferred wavelength (Eq. 25)	
v_p	Phase velocity of λ_c (Eq. 26)	
r	Growth rate of λ_c (Eq. 27)	

$$\frac{a\sigma_0'}{V_0}s^2 + \left[\frac{(a-b)\sigma_0'}{L} + \frac{G|k|H_1(s,k)}{2(1-\nu_u)} - ik\frac{BG}{3}\frac{1+\nu_u}{1-\nu_u}(f_0 - \alpha_{LD})H_2(s,k)\right]s +$$
$$\frac{V_0}{L}\left[\frac{G|k|H_1(s,k)}{2(1-\nu_u)} - ik\frac{BG}{3}\frac{1+\nu_u}{1-\nu_u}f_0 H_2(s,k)\right] = 0. \qquad (24)$$

The undrained limit, which was previously described ($ck^2/s \to 0$ and $\mathcal{F} < \infty$), is attained from Eq. 24 by setting $H_1 = H_2 = 1$.

3.2. Undrained limit

In order to gain insight into the stability of the fault we solve Eq. 24 for $s(k)$ with near-rate-neutral friction, $a - b = O(10^{-4})$ (Fig. 2). The figure reveals that a range of wavelengths is linearly unstable to small perturbations at mildly rate-strengthening friction. Unlike instabilities at the interface of two identical elastic half-spaces, there is a wavelength of maximum growth rate, which we will refer to as the **preferred wavelength**, noting that both larger and smaller wavelengths are stable. The stability at large wavelengths suggests pulse-like propagation, rather than crack-like expansion of slip instabilities. Further suggesting pulse-like behavior is the directional dependence of the solutions to Eq. 24, which assumes slip localization on $y > 0$ side of the fault core. The equation predicts that a perturbation with $k > 0$ (propagating to the right, as shown in Fig. 1c) experiences pore pressure changes that can overcome the otherwise stabilizing effects of mildly rate-strengthening friction, but perturbations with $k < 0$ (i.e., propagating to the left, not shown) have pressure changes that further stabilize sliding, due to the sign change in pore pressure (Eq. 15). This gives rise to directionality and determines the pulse propagation direction. For localization on the $y < 0$ side of the fault core, the characteristic equation is attained by changing the sign of the pore pressure terms (that is changing $-ik \to ik$ in Eq. 24). Then perturbations with $k < 0$ can be unstable under rate-strengthening friction, but $k > 0$ perturbations are always stable. This suggests that pulses may propagate in both directions on the same fault depending on where localization occurs. However, one direction may be favored if there are additional elastic bimaterial effects, as we discuss later.
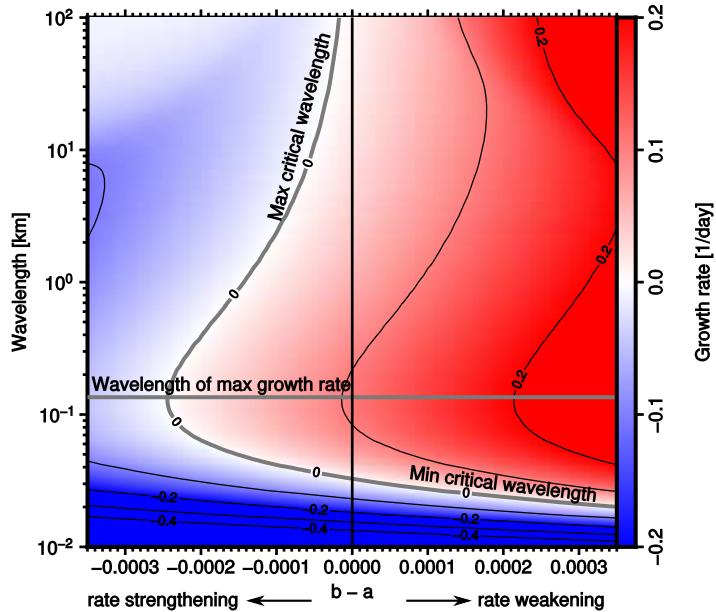
13

Figure 2: Growth/decay rate from linear stability analysis in the undrained limit, with the gray contour marking neutral stability. For rate-weakening friction ($b - a > 0$), all wavelengths greater than a critical wavelength are unstable. For rate-strengthening friction ($b - a < 0$), instability occurs for a range of wavelengths provided that $a - b$ is sufficiently small. The wavelength of maximum growth rate, also marked, is relatively independent of $a - b$. Parameters given in Table 1. See also Fig. 3.

239   If slip localizes in the fault core, but away from its boundaries, then the magnitude of
240 the pore pressure perturbation is reduced (Fig. 1b). Exactly in the center of the fault core
241 there is no perturbation in pore pressure, and this configuration is therefore linearly stable
242 at mildly rate-strengthening friction. The corresponding solution can be attained from Eq.
243 24 by setting $H_2 = 0$.

244   For simplicity and insight, we provide approximate expressions valid in the undrained
245 limit (negligible fluid flow) near rate-neutral friction ($a \sim b$) and assuming $\alpha_{LD} = 0$. We
246 observed from numerical solutions to Eq. 24 that $|\mathrm{Re}(s)| \ll |\mathrm{Im}(s)|$ near rate-neutral fric-
247 tion, meaning that the growth rate of perturbations is much smaller than their angular
248 frequency. Given these observations we assume the second order $\mathrm{Re}(s)^2$ term may be ig-
249 nored which results in explicit closed form solutions for $\mathrm{Re}(s)(k)$ and $\mathrm{Im}(s)(k)$, valid if

14

Re$(s)(k) \ll Im(s)(k)$. Then solving dRe$(s)(k)/dk = 0$ for k gives an approximate expression for the preferred wavenumber. Substituting this approximate expression in Re$(s)(k)$ and Im$(s)(k)$ provides growth rate and angular frequency evaluated at the preferred wavenumber. However, in spite of the $|$Re$(s)(k)| \ll |$Im$(s)(k)|$ assumption, these expressions are too complicated to provide insight into first order effects. We perform a Taylor expansion to leading order in Bf_0, recognizing that under most conditions Bf_0 is smaller than unity. This approximation of the preferred wavelength is

$$\lambda_c \equiv \frac{9\pi L G}{\sigma_0' a (1 + \nu_u)^2 (1 - \nu_u)(Bf_0)^2}. \tag{25}$$

Slip pulses propagate along the interface in the direction of strength reduction (Fig. 1c), and we gain insight into their propagation speed by deriving the approximate phase velocity, $v_p = -$Im$(s)/k$, at λ_c:

$$v_p \equiv \frac{3V_0 G}{2\sigma_0' a (1 + \nu_u)(1 - \nu_u)Bf_0}. \tag{26}$$

The approximate growth rate of λ_c is

$$r \equiv \frac{V_0}{L} \left[\frac{(Bf_0)^2}{18}(\nu_u + 1)^2 + \frac{b - a}{2a} \right]. \tag{27}$$

Equation 27 also quantifies the maximum rate-strengthening $a - b$ that can be destabilized by effective normal stress changes: $(a - b)_{\text{crit}} \approx a(1 + \nu_u)^2 (Bf_0)^2 / 9$.

3.3. Correspondence between undrained poroelastic and elastic bimaterial problems

The linear stability results for the elastic bimaterial problem[36, 38] are mathematically identical to those describing the undrained poroelastic problem (where $H_1 = H_2 = 1$), with the substitution $G/(1 - \nu_u) \to M$ and $2B(1 + \nu_u)/3 \to \beta$, where M and β are elastic bimaterial parameters defined by Rice et al.[36] to quantify elastic moduli and material contrast, respectively. Apparently, though, the connection between slow slip pulses and stability characteristics was overlooked in previous studies. The correspondence between undrained poroelastic sliding and the elastic bimaterial sliding goes beyond the stability characteristics since the relationships between sliding and fault stresses are also identical through the aforementioned substitution. For example, Eq. 14 becomes $\hat{\tau} = -(M/2)|k|\hat{\delta}$ and Eq. 15

15

gives $\hat{\sigma}' = (M\beta/2)ik\hat{\delta}$, which demonstrates a direct parallel between the two problems, at least when inertial and elastodynamic effects are negligible. This correspondence between quasi-static sliding of elastic bimaterial and undrained poroelastic interfaces has not been pointed out before to the best of our knowledge.

Note that for natural faults, β is typically less than 0.1 [36], while $B \approx 0.5$ to 0.9 [41]. Thus we conclude that destabilization by poroelastic effects is more likely to cause slow slip instabilities than elastic bimaterial effects on rate-strengthening faults, justifying our focus on the poroelastic instability numerical simulations.

It is worth noting that mildly rate-strengthening friction can also be destabilized during sliding on a interface between two identical elastic materials when the system lacks geometric reflection symmetry, a situation that can arise, for example, when sliding two plates of different thickness across one another[40]. However, these systems will possess additional length scales associated with the geometry (e.g., plate thickness) and thus are not generally mathematically equivalent to undrained poroelastic or elastic bimaterial sliding. [ELIAS, LET'S DISCUSS HOW TO REWRITE THIS.]

3.4. Stabilizing effects of diffusion and fluid flow

Both lateral diffusion and diffusion across the fault core will act to equilibrate poroelastic pressure changes. If this equilibration process occurs sufficiently fast, as compared to the growth time of the instability described in previous sections, then sliding will be stabilized. Here we identify two nondimensional parameters, γ and ϵ, that quantify the importance of lateral and across-fault diffusion, respectively.

To determine the time scales over which pressure equilibration occurs, we examine Eq. 17 that expresses pore pressure change on the fault. Pressure change vanishes if the function $H_2(s, k) \to 0$. This can occur if either ck^2/s (comparing Laplace parameter s to the diffusion time along the fault, $(k^2 c)^{-1}$) or $\mathcal{F}$ (quantifying across-fault pressure equilibration) is sufficiently large. Eq. 17 also reveals that the relative magnitude of ck^2/s and $\mathcal{F}$ determines which equilibration mechanism is dominant. If $\mathcal{F}/\sqrt{1 + s/ck^2} \ll 1$, then the fault core can be regarded as impermeable, so pressure equilibration occurs by lateral flow parallel to

16

the fault. This will stabilize the system if ck^2/s is sufficiently large. We thus deduce that instability requires that both $\mathcal{F}/\sqrt{1+s/ck^2} \ll 1$ and $ck^2/s \ll 1$. However, $s = s(k)$ is generally complex and therefore inappropriate for use in defining dimensionless parameters.

We therefore nondimensionalize s and k, first by generic time and length scales, then later by selecting these scales as those characterizing the maximum growth rate instability under undrained conditions. Let s^* and k^* be characteristic growth rate and wavenumber, respectively, such that in a relevant range the nondimensional growth rate $\tilde{s} = s/s^*$ and wavenumber $\tilde{k} = k/k^*$ are both of order unity. It follows that $ck^2/s = c(k^*)^2/s^* \times \tilde{k}^2/\tilde{s}$, where $\tilde{k}^2/\tilde{s}$ is of order unity. The nondimensional parameter is identified as $\gamma \equiv c(k^*)^2/s^*$, which is the ratio the time scale of lateral diffusion, $[(k^*)^2 c]^{-1}$ and the time scale of the instability $(s^*)^{-1}$. Instability is promoted by small values of γ.

Across-fault diffusion is negligible relative to lateral diffusion when $\mathcal{F}/\sqrt{1+s/ck^2} \ll 1$. To quantify the relative importance of these processes, we write $\mathcal{F} = 2\kappa_c/(\tilde{k}\kappa w k^*)$, from which we identify $\psi \equiv 2\kappa_c/\kappa w k^*$. Now $\sqrt{1+s/ck^2} \sim \sqrt{1+1/\gamma}$ and if $\gamma \ll 1$, as required for instability, then $\sqrt{1+1/\gamma} \approx \sqrt{1/\gamma}$. We then identify the nondimensional ratio that characterizes the competition between across-fault and lateral diffusion:

$$\epsilon \equiv \psi\sqrt{\gamma} = \frac{2\kappa_c}{\sqrt{\kappa}w}\sqrt{\frac{M}{s^*}}. \tag{28}$$

Instability is promoted by small values of ϵ.

Next we take $s^* = r$ in Eq. 27, with $a = b$ (rate-neutral friction), and $k^* = 2\pi/\lambda_c$ from Eq. 25. These scales are used to nondimensionalize results in Fig. 3. Fig. 3a and b show how stability at rate-neutral friction changes by systematically varying γ and ϵ, respectively, and solving Eq. 24 for $s = s(k)$. This comparison reveals that the choice of characteristic scales and nondimensional parameters is appropriate and the conditions $\epsilon, \gamma \ll 1$ yield the undrained response.

If $\epsilon \ll 1$, then the dominant diffusion mechanism is lateral and the fault core is effectively impermeable on relevant time scales, a necessary but not sufficient condition for instability. It is furthermore necessary that γ be sufficiently small such that lateral diffusion cannot stabilize the nucleation process. Interestingly, the condition on γ is far less restrictive than

17

$\gamma \ll 1$, as Fig. 3a shows instability even for γ several orders of magnitude larger than unity.

In addition, Fig. 3c compares the approximate solutions of Eqs. 25, 26, and 27, developed under the assumption that $Bf_0 \ll 1$, with numerical solutions to Eq. 24, showing good agreement even though $Bf_0 = 0.36$. There is a clear peak in growth rate $(\mathrm{Re}(\tilde{s}))$ in the vicinity of the preferred wavelength for both rate-strengthening and rate-weakening friction. However, at increasingly rate-weakening friction a more rapidly growing instability occurs at larger wavelengths. It is worth noting that in nature we could expect Bf_0 as large as $0.5 - 0.7$, where the premise of the expansion in Eqs. 25, 26, and 27 is questionable. In that case the reader may want to simply solve Eq. 24 to get a more accurate answer. However, we have found that the first order expansions are roughly correct up to a factor of 2 for $Bf_0 \approx 0.6$ and may thus still be useful.

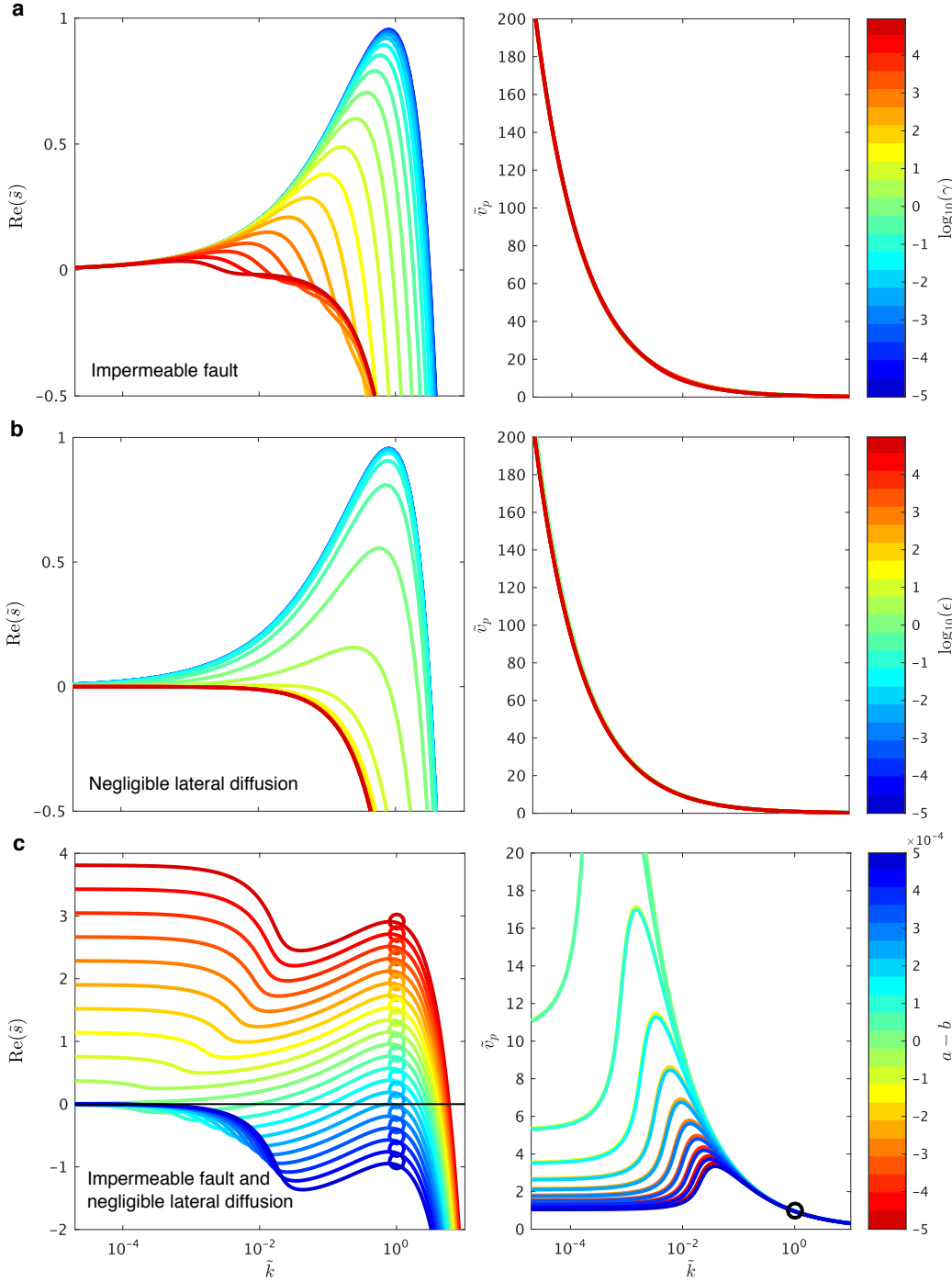Figure 3: Linear stability analysis results showing nondimensional growth rate $\mathrm{Re}(\tilde{s})$ and phase velocity $\tilde{v}_p$ as a function of nondimensional wavenumber $\tilde{k}$. We nondimensionalize k, v_p, and $\mathrm{Re}(s)$ by Eqs. 25, 26, and 27, respectively, with $a = b$. **a**, Fault core is impermeable ($\psi = 0$, and thus $\epsilon = 0$) but lateral diffusion is allowed by changing γ. Friction is rate-neutral ($a = b$). Phase velocity is largely independent of γ. **b**, Negligible lateral diffusion ($\gamma = 2.4 \times 10^{-6}$), but ϵ is varied to explore effects of across-fault flow. Friction is rate-neutral. **c**, Effectively undrained limit ($\gamma = 2.4 \times 10^{-6}$, $\epsilon = 0$) for various $a - b$. Circles indicate approximate values given by Eqs. 25, 26, and 27. Phase velocity depends on $a - b$, although near the preferred wavelength it is relatively constant. Different values of γ and ϵ are explored by altering the mobility parameters κ and κ_c, respectively; other parameters are as listed in Table 1.

19

4. Numerical simulations

In the previous section we presented a linearized analysis that is only strictly valid for small perturbations around steady state. Now we explore numerically how instabilities evolve once nonlinear effects become important.

4.1. Problem statement and numerical methodology

The linear poroelastic equations are solved using a finite difference method with summation-by-parts properties [44, 45]. Boundary conditions are enforced weakly using carefully chosen penalty terms [46] such that numerical stability can be established using the energy method. The numerical strategy follows [47] closely, using their fluid content formulation, but has been extended to allow for stretched grids and enforce displacement boundary conditions without approximating them by Robin conditions.

Simulations are conducted with a uniform grid spacing and periodic boundary conditions in the x direction. The sliding interface ($y = 0$) is assumed to be impermeable ($\partial p / \partial y = 0$). Assuming antisymmetry of displacement component u_x and symmetry of u_y about $y = 0$, together with no opening or interpenetration of material across the interface, there is no change in total normal stress σ_{yy} on the interface. We exploit these symmetries to model only the top poroelastic block, replacing interface conditions with boundary conditions. The third condition on the interface sets shear traction equal to the rate-and-state frictional strength. The top boundary, parallel to the sliding interface, is placed at $y = 7\lambda_c$. Boundary conditions on it are displacement at constant rate ($u_x = V_0 t / 2$), no normal displacement ($u_y = 0$), and no fluid flow through the boundary ($\partial p / \partial y = 0$). Results are relatively independent of the latter two conditions if the domain is sufficiently large. For computational efficiency, we applied a coordinate transformation in the y direction such that the grid spacing is finer near the fault and becomes ten times larger over a distance of $1.5\lambda_c$. The domain size in the x direction ranges from 17 to 50 times λ_c. Unless stated otherwise, we keep $\gamma = 0.08$ by varying the hydraulic diffusivity c, which ranges from 5×10^{-5} to $0.02 \text{ m}^2/\text{s}$. In comparison, relevant types of rock can have c in the range of 10^{-5} to $1 \text{ m}^2/\text{s}$ [41]. In the simulations we only explore the limit of a fully impermeable fault ($\epsilon = 0$). With regard to initial conditions,

₃₆₇ the block is subjected to shear strain such that the shear stress at the frictional interface is

₃₆₈ $\tau = f_0 \sigma'_0$, corresponding to steady sliding at slip rate V_0 if the initial state variable is also

₃₆₉ set equal to its steady state value. The far-field constant velocity loading ensures that as the

₃₇₀ fault slides at steady state the block moves without additional straining, thus maintaining

₃₇₁ constant shear stress at the interface. Perturbations to initial state variable are added to

₃₇₂ trigger departures from steady sliding and potentially sliding instability.

₃₇₃ *4.2. Spontaneous formation of slip pulses*

₃₇₄ Simulations with fully nonlinear rate-and-state friction response at mildly rate-strengthening

₃₇₅ friction support the interpretations of the linear stability analysis. Linear stability at larger

₃₇₆ wavelengths leads to slip pulses (Figs. 1c, 4, 5). Furthermore, we find that from slight

₃₇₇ white noise perturbations to a fault driven at steady state, there is selection of a wavelength

₃₇₈ of maximum growth rate which propagates along the fault with phase velocity; both the

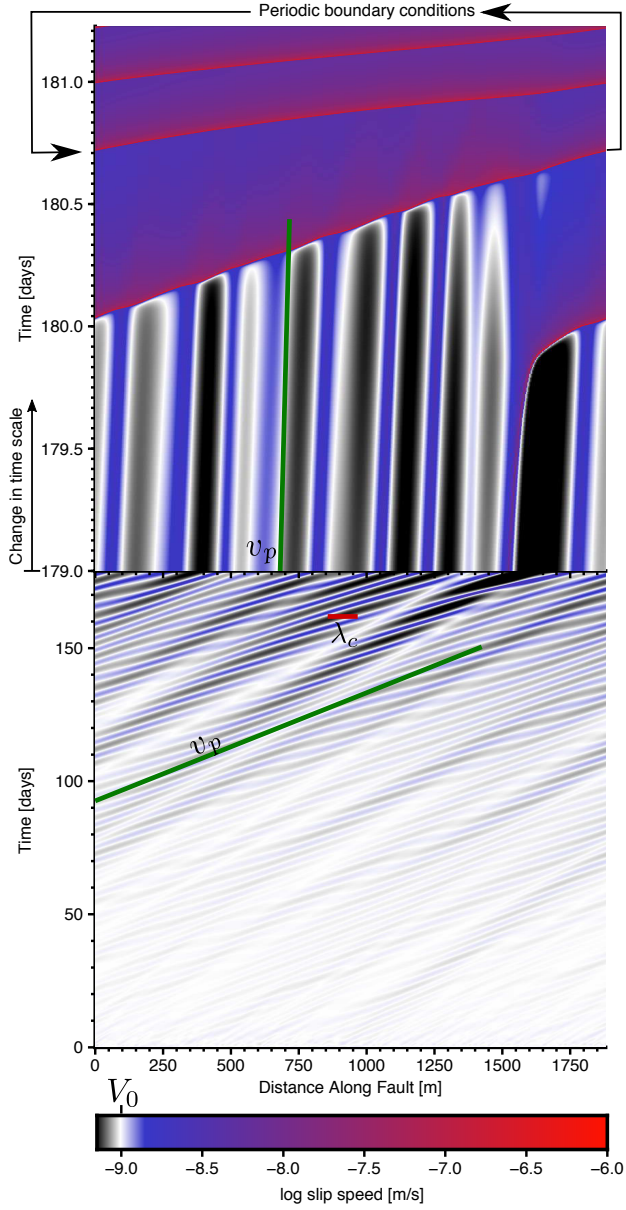₃₇₉ wavelength and phase velocity are in agreement with linear theory (Fig. 4).

21

Figure 4: Evolution of slip rate in a simulation of sliding between poroelastic blocks with rate-strengthening friction. Certain wavelength perturbations, seeded from random initial state conditions, grow in accordance with the linearized analysis until nonlinearities trigger slip pulse formation around 179-180 d (note change in time axis at 179 d). Continued propagation of the slip pulse smooths heterogeneities, and the system enters a steady, inhomogeneous sliding state with one active slip pulse (see also Fig. 1c). The approximate preferred wavelength λ_c (Eq. 25) and associated phase velocity v_p (Eq.26) from the linearized analysis are shown with red and green lines, respectively. Parameters given in Table 1.
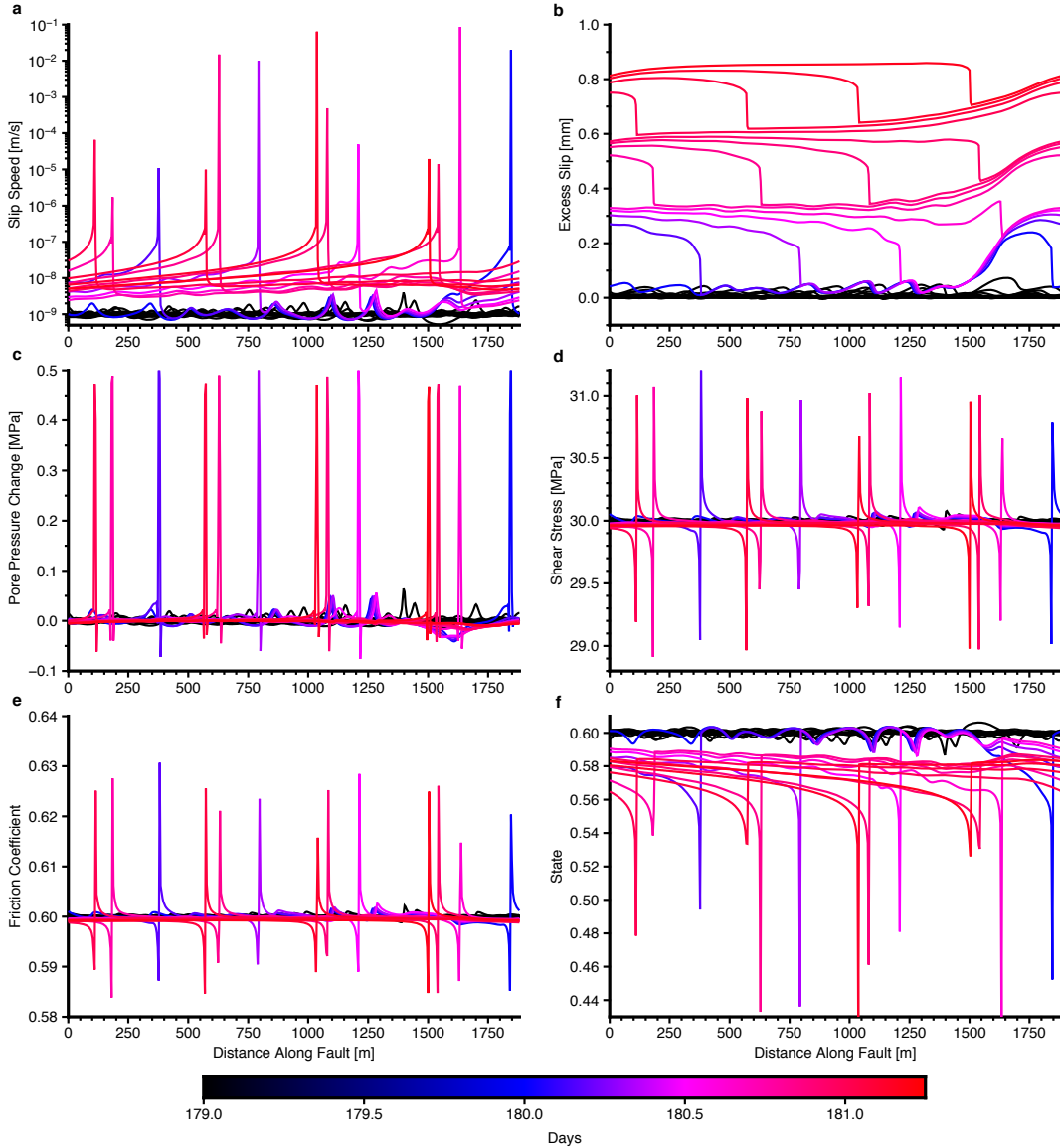
Figure 5: Snapshots of various fields on the sliding interface from the numerical simulation shown in Fig. 4. Lines that correspond to earlier times than day 179 (roughly the onset of the slip pulse) are black.

From investigating snapshots of various fields on the slip surface in the simulation in Fig. 4 we observe several important characteristics of the slip pulses. Firstly, the pulse slip in excess of steady state sliding is only about 0.3 mm (Fig. 5b). Secondly, the shear stress drop is only a fraction of a mega pascal. These are commonly observed characteristics of slow slip[48], which distinguish slow slip in nature from earthquakes. However these potential

23

³⁸⁵ observables depend on the assumed parameters, this dependence is explored in Fig. 6.

4.3. Slip pulse characteristics

³⁸⁷ Results from analysis of the linearized problem help explain parameter controls on pulse
³⁸⁸ length Λ_c and propagation speed V_p in the fully nonlinear simulations, though we find that
³⁸⁹ for the chosen parameters, slip pulses are 10 to 100 times longer and faster than predicted by
³⁹⁰ the linear theory. We quantify the characteristics of slip pulses in our numerical simulations
³⁹¹ (Fig. 6) as follows. The simulation domain is $50\lambda_c$ in x and $7\lambda_c$ in y. A region along the
³⁹² fault of length $3.5\lambda_c$ is perturbed about steady sliding to trigger instability. A slip pulse
³⁹³ forms and propagates into the unperturbed region, and its length Λ_c and propagation speed
³⁹⁴ V_p are measured. An example of this type of simulation is shown in Fig. 7. We define Λ_c as
³⁹⁵ the distance from the peak slip rate to where the slip rate has decayed to $1.5V_0$. The excess
³⁹⁶ slip is measured as the maximum average slip over the whole simulation domain in excess
³⁹⁷ of the background sliding. Similarly, the stress drop is measured as the maximum spatially
³⁹⁸ averaged shear stress drop during the simulation relative to the steady state stress, that is,

$$\Delta\tau = \max_t \frac{1}{l} \int_0^l \left[f_0\sigma_0' - \tau(x,t) \right] dx, \tag{29}$$

³⁹⁹ where l is the length of the simulation domain. These definitions of stress drop and excess
⁴⁰⁰ slip, while different than standard seismological definitions, are appropriate for a spatially
⁴⁰¹ periodic system with steady external loading. Some variability in slip pulse characteristics
⁴⁰² is observed when changing how the fault is initially perturbed or altering the domain size
⁴⁰³ (which can affect how many pulses nucleate and are simultaneously active). However, this
⁴⁰⁴ variability is relatively minor, and the approach outlined here gives consistent results that
⁴⁰⁵ can be compared in a meaningful manner.

⁴⁰⁶ Generally speaking, we find that the expressions for preferred wavelength and associated
⁴⁰⁷ phase velocity from the linearized analysis correctly predict parameter combinations that
⁴⁰⁸ determine slip pulse length and propagation speed. Furthermore, we see that stress drop
⁴⁰⁹ and excess slip depend on assumed parameters (Fig. 6c and d). For example, larger L
⁴¹⁰ results in larger excess slip, and higher σ_0' results in a higher stress drop.
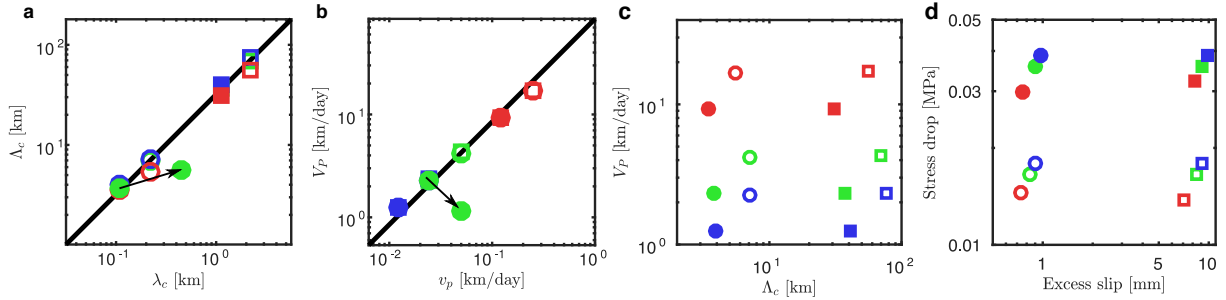
24

Figure 6: Comparison of simulated slip pulse characteristics with linear theory. **a** Slip pulse length Λ_c is proportional to the preferred wavelength λ_c from the linear theory (Eq. 25), with approximate relationship $\Lambda_c \approx 32\lambda_c$ (black line). **b** Slip pulse propagation speed V_p is proportional to phase velocity of the preferred wavelength from the linear theory (Eq. 26), with approximate relationship $V_P \approx 85v_p$ (black line). **c** Cross-plot of slip pulse length and propagation speed. **d** Same as **c** for stress drop and slip. In all panels, symbols/colors indicate parameter variations: Circles, $L = 10$ μm; squares $L = 100$ μm. Filled symbols, $\sigma_0' = 50$ MPa; open symbols, $\sigma_0' = 25$ MPa. Blue, $V_0 = 5 \times 10^{-7}$ mm/s; green, $V_0 = 10^{-6}$ mm/s; red, $V_0 = 5 \times 10^{-6}$ mm/s. Arrow shows how changing $Bf_0 = 0.36$ to 0.18 for one simulation alters the scaling between linear and nonlinear characteristics, suggesting more complex dependence on Bf_0 than predicted by linear theory. Other parameters given in Table 1.

4.4. Mildly rate-weakening friction

In this study we have focused primarily on simulations with mildly rate-strengthening friction, but it is worth commenting on the character of nonlinear slip behavior for rate-weakening friction. In Figs. 2 and 3c we observe at mildly rate-weakening friction ($b - a = O(10^{-4})$) that very large wavelengths become unstable. These unstable wavelengths are relatively independent of poroelastic processes and will remain unstable even if γ or ϵ are large. These wavelengths will, therefore, likely cause seismic or inertially limited events, assuming that the fault is sufficiently large to host such wavelengths. However, it is not clear at mildly rate-weakening friction if all wavelengths will generate seismic events or manifest as slow slip pulses. Preliminary nonlinear simulations under mildly rate-weakening friction (not shown here) suggest that mildly rate-weakening friction also produces stable slow slip pulses. These simulations, done with periodic boundary conditions, may simply not have a large enough domain to activate wavelengths capable of producing seismic events. We suggest that a fruitful topic of future research may focus on investigating the partition

25

of wavelengths capable of producing seismic events or slow slip. This could shed light on the potential transition from slow slip to seismic events.

5. Discussion

5.1. Experiments on hydrogels

Laboratory hydrogel experiments[8, 7, 9, 10, 11] have demonstrated sliding instabilities and slow slip pulses that are possibly explained by our mechanism. A poroelastic gel block is slid across a glass substrate, which may activate both poroelastic and elastic bimaterial destabilizing effects. Consistent with our predictions, steady sliding transitions spontaneously into slip pulses that advance, in the direction of motion of the gel block, at speeds much slower than wave speeds but several orders of magnitude faster than the driving speed V_0. In particular, experiments in an annular geometry[7], somewhat like our simulations with periodic boundary conditions, show evolution to a steady, inhomogeneous sliding state (Fig. 7) with direct proportionality between pulse speed and V_0 (c.f., Eq. 26). Moreover, the pulse length is independent of V_0 (c.f., Eq. 25).
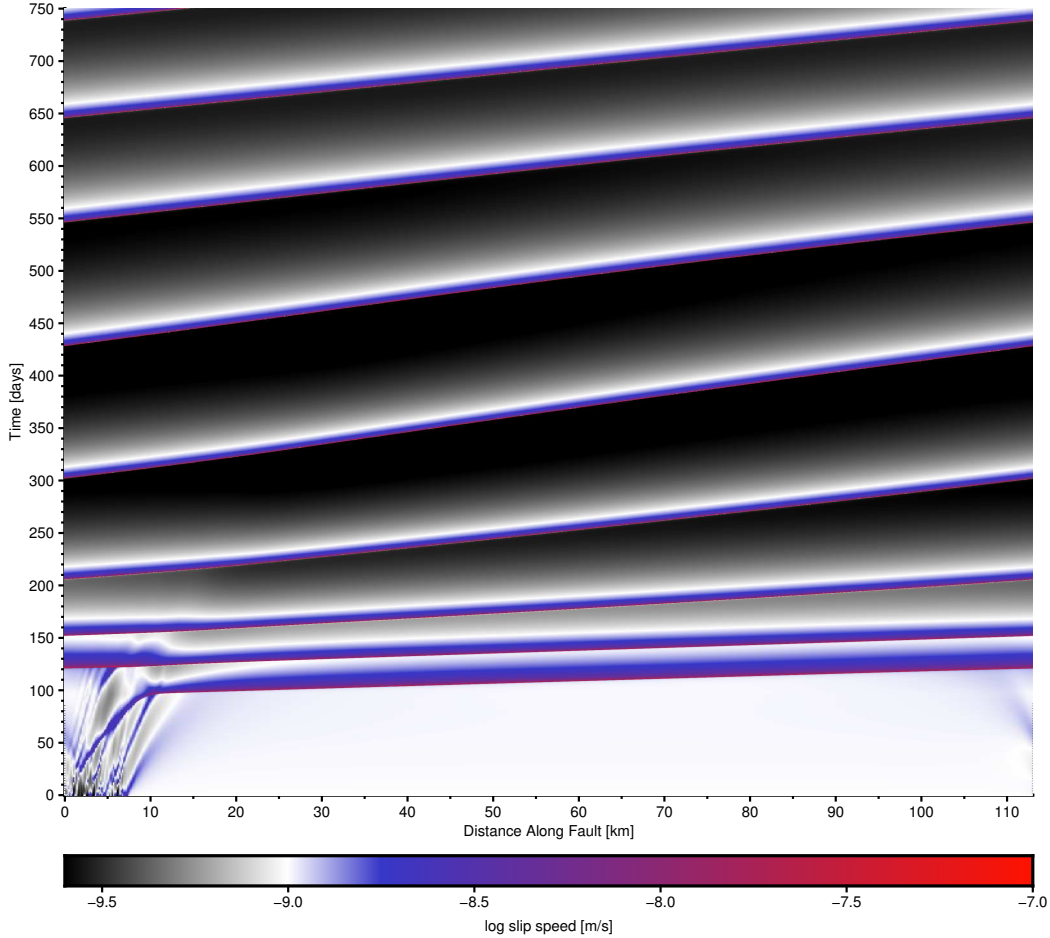
Figure 7: Evolution of slip rate in a simulation, similar to that shown in Figs. 4 and 5, but started from spatially localized perturbations in state $(0 < x < 3.5\lambda_c)$. The simulation is run for longer, until the system evolves to steady, inhomogeneous sliding with one (or more) active slip pulses. This is an example of a simulation that is used to characterize slip pulse characteristics reported in Fig. 6. Parameters here correspond to open green squares in Fig. 6.

439   Sliding of gel on glass features a dramatic contrast in elastic moduli, and thus one
440 might expect that the elastic bimaterial effect is dominant. However, many gels are nearly
441 incompressible. Experiments on gelatine suggest that the undrained Poisson's ratio $\nu_u \approx 0.5$,
442 but a drained value $\nu \approx 0.45$ [49]. This indicates that the elastic bimaterial coefficient β
443 (defined in section 3.3 and quantifying normal stress changes from nonuniform slip) ranges
444 from 0 to 0.1 [36], with $\beta = 0$ if the gel is completely incompressible. In contrast, Skempton's

27

445 coefficient $B \approx 1$ (Eq. 5) and hence the poroelastic coupling may cause larger changes in

446 effective normal stress than elastic bimaterial effects if our treatment of the interface effective

447 normal stress is valid for these systems. It may be that both effects contribute, as well as

448 coupling of slip to normal stress that arises from the lack of geometric reflection symmetry

449 [40] that is likely present in many hydrogel experiments.

450 One important observation of gel-on-glass sliding is that above a critical loading velocity

451 a homogeneous sliding mode set in and no slip pulses nucleate [9, 10]. An explanation of this

452 critical velocity has been offered using the framework of fracture mechanics, a linear viscous

453 friction law, and by drawing a comparison to first-order phase transitions[50]. Our analysis

454 does not directly explain this critical loading velocity, but it is worth noting that hydrogels

455 have a complex and often non-monotonic frictional strength at different slip speeds[51]. This

456 suggests that $a-b$ depends on velocity, and if the gel becomes sufficiently rate-strengthening

457 at a certain velocity, the instability we have identified would be suppressed.

458 We recognize that hydrogel experiments demonstrate several qualitative characteristics

459 that agree with our theoretical findings, but that the mechanical response of hydrogels

460 involves processes not present in our model. These include viscoelasticity, spatial finiteness,

461 edge effects, and possibly interface adhesion. Further study is needed to determine if we have

462 identified the right destabilization mechanism that manifests in these hydrogel experiments.

5.2. Potential application to subduction zone slow slip

464 We propose that our mechanism could be applied to subduction zone slow slip. However,

465 any true 3-D manifestations of this mechanism are hypothetical at this point and require

466 further study. Direct application of our 2-D simulations to subduction zones is complicated

467 by the 3-D nature of subduction slow slip, where slower migration along strike (i.e., in

468 the invariant dimension in our simulations) is interspersed with faster along-dip transients

469 [52, 53]. Our instability mechanism would act only in the along-dip (mode II) direction,

470 but along-strike (mode III) migration might be driven by stress transfer from currently

471 slipping sections of the interface that activates instability in adjacent sections (Fig. 8).

472 Furthermore, instabilities might also arise behind the main slip front and are predicted to

28

propagate along-dip at higher velocities due to the accelerated sliding rate (c.f., Eq. 26). Similar ideas have been previously proposed based on tremor observations and geodetic modeling that suggest the large scale slow slip is, in reality, the manifestation of many slow transients[54]. It is worth noting that tremors migrate both up and down dip in subduction zones[53]. The poroelastic mechanism can explain both directions since the directionality is simply determined by in which side of the fault core slip localization occurs. However, a bimaterial destabilizing mechanism cannot explain migration in both directions.

The migration of tremor along the dip direction in subduction zones has been inferred to be faster than in simulations in the paper (Fig. 6). For example, in Japan they are around 25 to 250 km/h compared to the along-strike migration of $\sim$10 km/d [55]. Similar migration speeds of low frequency tremor are also observed on strike slip faults in the in-plane direction of sliding[56].

The mechanism we have presented can potentially explain the along-dip migration rates as large as observed in Japan and elsewhere if effective normal stress is sufficiently low. Indeed, previous authors have suggested that the effective normal stress may be around 0.1 MPa[57]. The effective normal stress in most simulations in this study has been $\sim$50 MPa, which results in propagation speed of about $\sim$0.1 km/h. This is $\sim$100 to 1000 times slower than the previously mentioned values for Japan. To test if comparable propagation speeds are observed in simulations at low effective normal stress, we ran two additional simulations at $\sigma'_0 = 1$ MPa and 0.1 MPa, but otherwise with reference parameters in Table 1. The setup of these simulations is otherwise the same as in Section 4.3. The low effective stress simulations reveal $V_P = 800$ km/d $= 33$ km/h for $\sigma'_0 = 0.1$ MPa and $V_P = 140$ km/d $= 5.8$ km/h for $\sigma'_0 = 1$ MPa. This demonstrates that at low effective normal stress the simulations predict the right order of magnitude for the tremor migration speeds observed in nature. Furthermore, the simulations at low effective normal stress show that the inferred relationship $V_p \approx 85 v_p$ in Fig. 6 still holds reasonably well.
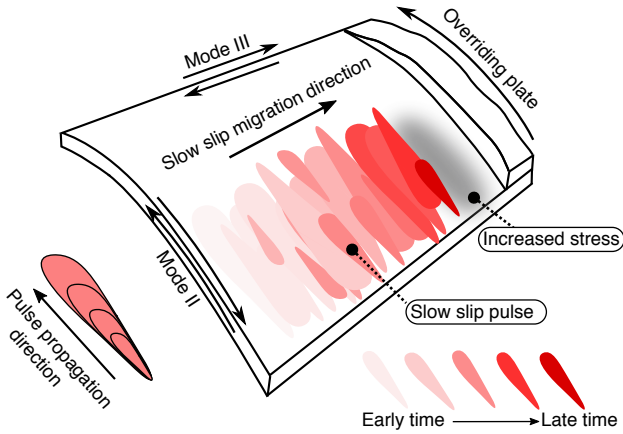
Figure 8: Schematic illustrating slip pulse instability in mode II direction, with mode III propagation driven by stress transfer.

Slow slip can also occur in the shallow parts of subduction zones, where experiment on rock samples have confirmed rate-strengthening behavior [18]. These regions may combine three processes that can destabilize rate-strengthening friction: poroelastic coupling, elastic bimaterial contrast, and lack of geometric reflection symmetry[58, 40]. All these processes may act simultaneously and should be considered in mechanical models of shallow subduction zone processes such as slow slip events and tsunami earthquakes[59].

5.3. Further applicability

Our results might also apply to other problems. These include magnitude 7 slow slip events of the Whillans Ice Plain[60], an Antarctic ice stream sliding on rate-neutral glacial till[61], and slow, episodic advance of landslide masses[62]. Finally, in the context of reservoir geomechanics, if fault/fracture networks have heterogeneous frictional properties, the advance of slow slip along a rate-strengthening fault might manifest as a swarm of small earthquakes that migrates at relatively constant speed. Microseismic swarms accompanying fluid injection (e.g., in oil/gas operations) can indeed migrate faster than can be explained by pore pressure diffusion, possibly as a consequence of aseismic slip[6, 63]. Additionally, the possibility of slow slip with rate-strengthening friction brings more consistency to the

hypothesized role of slow slip in reservoir stimulation (permeability enhancement by fluid injection and hydraulic fracturing)[5]. Reservoir rocks such as shales contain clays and organics that are experimentally linked to rate-strengthening behavior[17]. The reservoir setting might also be ideal for model validation through direct measurements of pore pressure changes on or adjacent to faults concurrently with slip using recently developed borehole instruments[6].

6. Conclusions

We have investigated spontaneously occurring sliding instabilities that occur with mildly rate-strengthening friction due to the coupling of slip and effective normal stress via two different mechanisms. These instabilities are fundamentally different from standard earthquake-inducing instabilities with rate-weakening friction in that they are characterized by a preferred wavelength having a maximum growth rate, with stability at both smaller and larger wavelengths, and a strong preference in propagation direction. Simulations with nonlinear rate-and-state friction show that these instabilities become slow slip pulses and are broadly consistent with many aspects of slow slip in nature, such as low stress drops and small slip distances. Furthermore, we find quantitatively similar propagation speeds of pulses as compared to tectonic tremor and geodetically inferred slow slip migration speeds under low effective normal stress conditions. We also observe qualitative consistency with slow slip pulses identified in experiments on hydrogels. We have proposed a conceptual model for how this type of instability might manifest in 3-D in a subduction zone setting, where unstable pulses propagate in the along-dip (mode II) direction and along-strike (mode III) migration is driven by secondary stress transfer due to cascading of pulses. However, we recognize that in order to make a full comparison to slow slip in experiments and geological settings we need to understand how the reported frictional instabilities manifest in three dimensions. In summary, our work demonstrates how poroelastic and elastic bimaterial effects can destabilize mildly rate-strengthening sliding to generate slow slip events having features consistent with observations.

7. Acknowledgements

Declaration of Interest

None

Appendix A. Poroelastic solution

This appendix outlines the derivation of the linear relations between shear stress change and slip and pore pressure change and slip that are implemented in deriving the characteristic equation 24.

We solve Eqs. 1 and 2 using the method of displacement functions[64, 65], which are a special case of the Biot potentials[66] applicable to plane strain problems. In order to find the displacement functions, $\mathcal{S}$ and $\mathcal{E}$, we solve

$$\nabla^2 \mathcal{S} = 0, \tag{A.1}$$

$$\frac{\partial}{\partial t}(\nabla^2 \mathcal{E}) - c\nabla^4 \mathcal{E} = 0. \tag{A.2}$$

By Fourier transforming with respect to x, with wavenumber k, and Laplace transforming in time, with Laplace parameter s, the problem is reduced to ordinary differential equations

32

in y. Transformed fields are denoted as $\hat{p}$ for p, etc. The transformed equations can be solved analytically. Disregarding the solution terms that diverge at infinity, we find

$$\hat{\mathcal{E}}^{\pm} = C_1^{\pm} \exp(\pm|k|y) + C_2^{\pm} \exp(\pm\sqrt{k^2 + s/c}y), \tag{A.3}$$

$$\hat{\mathcal{S}}^{\pm} = C_3^{\pm} \exp(\pm|k|y), \tag{A.4}$$

where $C_1^{\pm}$, $C_2^{\pm}$, and $C_3^{\pm}$ are determined by interface conditions. Transforming the displacements functions into physical fields give the displacements and pore pressure as [41]

$$\hat{u}_x^{\pm} = -ik\hat{\mathcal{E}}^{\pm} + iky\hat{\mathcal{S}}^{\pm}, \tag{A.5}$$

$$\hat{u}_y^{\pm} = -\frac{\partial\hat{\mathcal{E}}^{\pm}}{\partial y} + y\frac{\partial\hat{\mathcal{S}}^{\pm}}{\partial y} - (3 - 4\nu_u)\hat{\mathcal{S}}^{\pm}, \tag{A.6}$$

$$\hat{p}^{\pm} = -G\frac{2(1-\nu)}{\alpha(1-2\nu)}\left[-k^2\hat{\mathcal{E}}^{\pm} + \frac{\partial^2\hat{\mathcal{E}}^{\pm}}{\partial y^2} - \frac{2(\nu_u - \nu)}{1-\nu}\frac{\partial\hat{\mathcal{S}}^{\pm}}{\partial y}\right]. \tag{A.7}$$

The stresses σ_{ij} are obtained from Hooke's law,

$$\sigma_{ij} = 2G\epsilon_{ij} + \frac{2G\nu}{1-2\nu}\epsilon_{kk}\delta_{ij} - \alpha p\delta_{ij}, \tag{A.8}$$

where δ_{ij} is the Kronecker delta and ϵ_{ij} is the strain tensor, relevant transformed components of which are written as $\hat{\epsilon}_{xx}^{\pm} = ik\hat{u}_x^{\pm}$ and $\hat{\epsilon}_{xy}^{\pm} = (ik\hat{u}_y^{\pm} + \hat{u}_{x,y}^{\pm})/2$, for example.

The $C_1^{\pm}$, $C_2^{\pm}$, and $C_3^{\pm}$ are then determined using a symbolic manipulator where the appropriate boundary conditions are matched (Sections 2.2 and 2.3). Then the pore pressure and shear stress are computed at the interface $y \to 0^{\pm}$, which finally grants expressions presented in Section 3.1.

References

[1] I. Svetlizky, J. Fineberg, Classical shear cracks drive the onset of dry frictional motion, Nature 509 (7499) (2014) 205. doi:10.1038/nature13202.

[2] C. Marone, Laboratory-derived friction laws and their application to seismic faulting, Annu. Rev. Earth Pl. Sc. 26 (1) (1998) 643–696.

[3] Z. Peng, J. Gomberg, An integrated perspective of the continuum between earthquakes and slow-slip phenomena, Nat. Geosci. 3 (9) (2010) 599. doi:10.1038/ngeo940.

[4] G. C. Beroza, S. Ide, Slow earthquakes and nonvolcanic tremor, Annu. Rev. Earth Pl. Sc. 39 (1) (2011) 271–296. doi:10.1146/annurev-earth-040809-152531.

[5] M. D. Zoback, A. Kohli, I. Das, M. W. Mcclure, The importance of slow slip on faults during hydraulic fracturing stimulation of shale gas reservoirs, in: SPE Americas Unconventional Resources Conference, Society of Petroleum Engineers, 2012.

[6] Y. Guglielmi, F. Cappa, J.-P. Avouac, P. Henry, D. Elsworth, Seismicity triggered by fluid injection–induced aseismic slip, Science 348 (6240) (2015) 1224–1226. doi:10.1126/science.aab0476.

[7] J. Galeano, P. Espanol, M. Rubio, Experimental and theoretical results of stress relaxations in a model of earthquake dynamics, Europhys. Lett. 49 (4) (2000) 410.

[8] M. A. Rubio, J. Galeano, Stick-slip dynamics in the relaxation of stresses in a continuous elastic medium, Phys. Rev. E 50 (2) (1994) 1000.

[9] T. Baumberger, C. Caroli, O. Ronsin, Self-healing slip pulses along a gel/glass interface, Phys. rev. lett. 88 (7) (2002) 075509.

[10] T. Baumberger, C. Caroli, O. Ronsin, Self-healing slip pulses and the friction of gelatin gels, Eur. Phys. J. E 11 (1) (2003) 85–93.

[11] O. Ronsin, T. Baumberger, C. Hui, Nucleation and propagation of quasi-static interfacial slip pulses, J. Adhesion 87 (5) (2011) 504–529.

[12] N. Kato, A possible model for large preseismic slip on a deeper extension of a seismic rupture plane, Earth Planet. Sc. Lett. 216 (1-2) (2003) 17–25.

[13] A. M. Rubin, Episodic slow slip events and rate-and-state friction, J. Geophys. Res. Solid Earth 113 (B11). doi:10.1029/2008JB005642.

[14] P. Segall, A. M. Rubin, A. M. Bradley, J. R. Rice, Dilatant strengthening as a mechanism for slow slip events, J. Geophys. Res. Solid Earth 115 (B12).

[15] Y. Bar-Sinai, E. A. Brener, E. Bouchbinder, Slow rupture of frictional interfaces, Geophys. Res. Lett. 39 (3). doi:10.1029/2011GL050554.

[16] Y. Bar-Sinai, R. Spatschek, E. A. Brener, E. Bouchbinder, On the velocity-strengthening behavior of dry friction, J. Geophys. Res. Solid Earth 119 (3) (2014) 1738–1748. doi:10.1002/2013JB010586.

[17] A. H. Kohli, M. D. Zoback, Frictional properties of shale reservoir rocks, J. Geophys. Res. Solid Earth 118 (9) (2013) 5109–5125. doi:10.1002/jgrb.50346.

[18] M. J. Ikari, C. Marone, D. M. Saffer, A. J. Kopf, Slip weakening as a mechanism for slow earthquakes, Nat. Geosci. 6 (6) (2013) 468. doi:10.1038/ngeo1818.

[19] D. M. Saffer, L. M. Wallace, The frictional, hydrologic, metamorphic and thermal habitat of shallow

34

613   slow earthquakes, Nat. Geosci. 8 (8) (2015) 594. doi:10.1038/ngeo2490.

614 [20] R. Bürgmann, The geophysics, geology and mechanics of slow fault slip, Earth Planet. Sc. Lett. 495
615   (2018) 112–134.

616 [21] J. R. Rice, D. A. Simons, The stabilization of spreading shear faults by coupled deformation-
617   diffusion effects in fluid-infiltrated porous materials, J. Geophys. Res. 81 (29) (1976) 5322–5334.
618   doi:10.1029/JB081i029p05322.

619 [22] J. R. Rice, M. P. Cleary, Some basic stress diffusion solutions for fluid-saturated elastic porous media
620   with compressible constituents, Rev. Geophys. 14 (2) (1976) 227–241. doi:10.1029/RG014i002p00227.

621 [23] J. W. Rudnicki, D. A. Koutsibelas, Steady propagation of plane strain shear cracks on an impermeable
622   plane in an elastic diffusive solid, Int. J. Solids Struct. 27 (2) (1991) 205–225.

623 [24] J. Weertman, Unstable slippage across a fault that separates elastic media of different elastic constants,
624   J. Geophys. Res. Solid Earth 85 (B3) (1980) 1455–1461.

625 [25] F. M. Chester, J. P. Evans, R. L. Biegel, Internal structure and weakening mechanisms of the san
626   andreas fault, J. Geophys. Res. 98 (B1) (1993) 771–786.

627 [26] J. S. Caine, J. P. Evans, C. B. Forster, Fault zone architecture and permeability structure, Geology
628   24 (11) (1996) 1025–1028.

629 [27] C. A. Wibberley, T. Shimamoto, Internal structure and permeability of major strike-slip fault zones:
630   the Median Tectonic Line in Mie Prefecture, Southwest Japan, J. Struct. Geol. 25 (1) (2003) 59–78.

631 [28] J. Behnsen, D. Faulkner, Water and argon permeability of phyllosilicate powders under medium to
632   high pressure, Earth Planet. Sc. Lett. 116 (B12).

633 [29] F. Chester, J. M. Logan, Implications for mechanical properties of brittle faults from observations of
634   the punchbowl fault zone, california, Pure Appl. Geophys. 124 (1-2) (1986) 79–106.

635 [30] T. Mitchell, D. Faulkner, Towards quantifying the matrix permeability of fault damage zones in low
636   porosity rocks, Earth Planet. Sc. Lett. 339 (2012) 24–31.

637 [31] F. M. Chester, J. S. Chester, Ultracataclasite structure and friction processes of the punchbowl
638   fault, San Andreas system, California, Tectonophysics 295 (1) (1998) 199 – 221. doi:10.1016/S0040-
639   1951(98)00121-8.

640 [32] F. M. Chester, J. S. Chester, D. L. Kirschner, S. E. Schulz, J. P. Evans, Structure of large-displacement,
641   strike-slip fault zones in the brittle continental crust, Rheology and deformation in the lithosphere at
642   continental margins 1 (2004) 223–260.

643 [33] O. Dor, T. K. Rockwell, Y. Ben-Zion, Geological observations of damage asymmetry in the structure of
644   the San Jacinto, San Andreas and Punchbowl faults in Southern California: A possible indicator for pre-
645   ferred rupture propagation direction, Pure Appl. Geophys. 163 (2) (2006) 301–349. doi:10.1007/s00024-
646   005-0023-9.

[34] J. W. Rudnicki, J. R. Rice, Effective normal stress alteration due to pore pressure changes induced by dynamic slip propagation on a plane between dissimilar materials, J. Geophys. Res. Solid Earth 111 (B10). doi:10.1029/2006JB004396.

[35] E. M. Dunham, J. R. Rice, Earthquake slip between dissimilar poroelastic materials, J. Geophys. Res. Solid Earth 113 (B9), b09304. doi:10.1029/2007JB005405.

[36] J. R. Rice, N. Lapusta, K. Ranjith, Rate and state dependent friction and the stability of sliding between elastically deformable solids, J. Mech. Phys. Solids 49 (9) (2001) 1865–1898.

[37] E. A. Brener, M. Weikamp, R. Spatschek, Y. Bar-Sinai, E. Bouchbinder, Dynamic instabilities of frictional sliding at a bimaterial interface, J. Mech. Phys. Solids 89 (2016) 149–173.

[38] M. Aldam, S. Xu, E. A. Brener, Y. Ben-Zion, E. Bouchbinder, Nonmonotonicity of the frictional bimaterial effect, J. Geophys. Res. Solid Earth 122 (10) (2017) 8270–8284.

[39] H. Shlomai, J. Fineberg, The structure of slip-pulses and supershear ruptures driving slip in bimaterial friction, Nat. Commun. 7 (2016) 11787.

[40] M. Aldam, Y. Bar-Sinai, I. Svetlizky, E. A. Brener, J. Fineberg, E. Bouchbinder, Frictional sliding without geometrical reflection symmetry, Phys. Rev. X 6 (2016) 041023. doi:10.1103/PhysRevX.6.041023.

[41] E. Detournay, A. H.-D. Cheng, Fundamentals of poroelasticity, in: Analysis and Design Methods, Elsevier, 1995, pp. 113–171.

[42] Y. Song, J. W. Rudnicki, Plane-strain shear dislocation on a leaky plane in a poroelastic solid, J. Appl. Mech. 84 (2) (2017) 021008.

[43] M. F. Linker, J. H. Dieterich, Effects of variable normal stress on rock friction: Observations and constitutive equations, J. Geophys. Res. Solid Earth 97 (B4) (1992) 4923–4940. doi:10.1029/92JB00017.

[44] M. Svärd, J. Nordström, Review of summation-by-parts-operators schemes for initial-boundary-value problems, J. Comput. Phys. 268 (0) (2014) 17–38.

[45] D. C. Del Rey Fernández, J. E. Hicken, D. W. Zingg, Review of summation-by-parts operators with simultaneous approximation terms for the numerical solution of partial differential equations, Comput. Fluids 95 (2014) 171 – 196.

[46] M. H. Carpenter, D. Gottlieb, S. Abarbanel, Time-stable boundary conditions for finite-difference schemes solving hyperbolic systems: Methodology and application to high-order compact schemes, J. Comput. Phys. 111(2) (1994) 220–236.

[47] K. Torberntsson, V. Stiernström, K. Mattsson, E. M. Dunham, A finite difference method for earthquake sequences in poroelastic solids, Computat. Geosci. 22 (5) (2018) 1351–1370. doi:10.1007/s10596-018-9757-1.

[48] H. Gao, D. A. Schmidt, R. J. Weldon, Scaling relationships of source parameters for slow slip events, Bull. Seismol. Soc. Am 102 (1) (2012) 352–360.

[49] R. Righetti, J. Ophir, S. Srinivasan, T. A. Krouskop, The feasibility of using elastography for imaging the poisson's ratio in porous media, Ultrasound Med. Biol. 30 (2) (2004) 215 – 228. doi:10.1016/j.ultrasmedbio.2003.10.022.

[50] E. A. Brener, S. V. Malinin, V. I. Marchenko, Fracture and friction: Stick-slip motion, Eur. Phys. J. E. 17 (1) (2005) 101–113. doi:10.1140/epje/i2004-10112-3.

[51] J. P. Gong, Friction and lubrication of hydrogelsits richness and complexity, Soft matter 2 (7) (2006) 544–552. doi:10.1039/B603209P.

[52] A. Ghosh, J. E. Vidale, J. R. Sweet, K. C. Creager, A. G. Wech, H. Houston, E. E. Brodsky, Rapid, continuous streaking of tremor in Cascadia, Geochem. Geophy. Geosy. 11 (12).

[53] Y. Peng, A. M. Rubin, High-resolution images of tremor migrations beneath the Olympic peninsula from stacked array of arrays seismic data, Geochem. Geophy. Geosy. 17 (2) (2016) 587–601. doi:10.1002/2015GC006141.

[54] W. B. Frank, B. Rousset, C. Lasserre, M. Campillo, Revealing the cluster of slow transients behind a large slow slip event, Sci. Adv. 4 (5). doi:10.1126/sciadv.aat0661.

[55] D. R. Shelly, G. C. Beroza, S. Ide, Complex evolution of transient slip derived from precise tremor locations in western shikoku, japan, Geochem. Geophy. Geosy. 8 (10). doi:10.1029/2007GC001640.

[56] D. R. Shelly, Migrating tremors illuminate complex deformation beneath the seismogenic san andreas fault, Nature 463 (7281) (2010) 648.

[57] R. Nakata, N. Suda, H. Tsuruoka, Non-volcanic tremor resulting from the combined effect of Earth tides and slow slip events, Nat, Geosci. 1 (10) (2008) 676.

[58] J. W. Rudnicki, M. Wu, Mechanics of dip-slip faulting in an elastic half-space, J. Geophys. Res. Solid Earth 100 (B11) (1995) 22173–22186. doi:10.1029/95JB02246.

[59] Y. Fukao, Tsunami earthquakes and subduction processes near deep-sea trenches, J. Geophys. Res. Solid Earth 84 (B5) (1979) 2303–2314. doi:10.1029/JB084iB05p02303.

[60] D. A. Wiens, S. Anandakrishnan, J. P. Winberry, M. A. King, Simultaneous teleseismic and geodetic observations of the stick–slip motion of an Antarctic ice stream, Nature 453 (7196) (2008) 770.

[61] N. R. Iverson, Shear resistance and continuity of subglacial till: hydrology rules, J. Glaciol. 56 (200) (2010) 1104–1114.

[62] W. H. Schulz, J. P. McKenna, J. D. Kibler, G. Biavati, Relations between hydrology and velocity of a continuously moving landslide-Evidence of pore-pressure feedback regulating landslide motion?, Landslides 6 (3) (2009) 181–190.

[63] P. Bhattacharya, R. C. Viesca, Fluid-induced aseismic fault slip outpaces pore-fluid migration, Science 364 (6439) (2019) 464–468. doi:10.1126/science.aaw7354.

[64] A. Verruijt, Displacement functions in the theory of consolidation or in thermoelasticity, Zeitschrift für

715   angewandte Mathematik und Physik ZAMP 22 (5) (1971) 891–898.

716   [65] J. McNamee, R. E. Gibson, Plane strain and axially symmetric problems of the consolidation of a

717   semi-infinite clay stratum, Q. J. Mech. Appl. Math. 13 (2) (1960) 210–227.

718   [66] M. A. Biot, General solutions of the equations of elasticity and consolidation for a porous material, J.

719   Appl. Mech. 23 (1) (1956) 91–96.